Analysis of Solid-State Reaction Mechanisms with Two-Dimensional FTIR Correlation Spectroscopy

Nataraju Bodappa,[a] Sarah Stepan,[a] Rodney D. L. Smith[a,b]*

[a]*Department of Chemistry, University of Waterloo, 200 University Avenue W., Waterloo, Ontario, Canada N2L 3G1*

[b]*Waterloo Institute for Nanotechnology, University of Waterloo, 200 University Avenue W., Waterloo, Ontario, Canada N2L 3G1*

Correspondence to:

rodsmith@uwaterloo.ca

ABSTRACT

The utility of two-dimensional generalized correlation spectroscopy (2D-COS) for tracking complex solid-state reactions is demonstrated using infrared spectra acquired during a photochemically-induced decomposition reaction. Eleven different thin films, consisting of 6 monometallic and 5 bimetallic 2-ethylhexanoate complexes, were tracked as a function of photolysis time. Overlapping peaks in the infrared fingerprint region are readily discriminated using 2D-COS, enabling individual vibrational components to be used to distinguish whether carboxylate ligands are free/ionic, or bound in chelating, bridging, or monodentate fashion. This classification enables the decomposition mechanism to be tracked for all 11 samples, revealing that ligands bound in monodentate and bridging fashion are first converted to chelates before being lost as volatile products for all samples. The magnitude of measured first-order rate constants for loss of chelated ligands is found to correlate linearly to the asymmetric stretching frequency of monodentate ligands but exhibit a V-shape when plotted against electronegativity of the metal center. We propose that loss of chelated ligands proceeds via C-O scission for highly electronegative transition metals but M-O scission for low electronegativity. These results establish 2D-COS as a powerful tool to deconvolute and correlate individual components, enabling mechanistic analysis for complex chemical reactions.

1. INTRODUCTION

Variation in fabrication protocols for solid-state materials can induce structural changes in the final materials that are challenging to identify but directly influence material properties. This poses a particular problem for highly disordered or defective materials that are finding use as electrocatalsyts,[1–3] where conventional structural characterization techniques such as X-ray diffraction have limited use and even state-of-the-art techniques provide only a limited amount of information. An example of this is seen in the comparison of structure and electrocatalytic behavior for disordered iron-nickel hydroxide materials, where similar electrochemical behavior but fundamentally different structural changes observed through X-ray absorption spectroscopy studies resulted in three different mechanistic interpretations.[1–3] A key difference between these reports is that each article utilized different fabrication protocols. Establishing techniques to identify and study the differences between similar materials synthesized through different routes is important because the number of synthetic techniques is rapidly expanding. The metal hydroxide materials at the center of the issue described above are routinely fabricated by a broad range of techniques, including cathodic[4–6] and anodic[7,8] electrodeposition, solution casting,[9] sputter deposition,[10] hydrothermal synthesis,[2] post-synthetic tuning,[11] pulsed laser abalation,[11,12] liquid phase exfoliation[13,14], photochemical irradiation[15] and ion-exchange methods.[16] Each of these approaches is likely to yield subtle variations in structural disorder that pose a challenge for analysis. This leads us to analyze the reaction mechanisms that lead to the final solid-state materials to gain insights into key characteristics of the final material.

Photochemically induced decomposition of metal-organic complexes has been presented as a means of synthesizing compositionally uniform thin-films of disordered metal hydroxides without requiring high temperatures.[15,17–19] Single transition metal precursors or arbitrary mixtures and stoichiometries of transition metals have been used to synthesize a range of electrocatalysts.[20–22] The loss of ligand C-H vibrations in Fourier transform infrared spectroscopy (FTIR) is readily used to monitor the decomposition of metal-organic complexes, and the mechanism of photochemical decomposition has been studied from the perspective of ligand decomposition, but little is known regarding the structural evolution of the transition metal centers. Mechanistic studies that analyzed gaseous products via GC-MS indicate that photolysis initiates a ligand-to-metal charge transfer (LMCT) process that results in heterolytic

cleavage of the carboxylate C-C bond, a subsequent release of CO_2, and cross-coupling between radicals to yield volatile organic products and a metal film that reacts with oxygen to yield a metal oxide thin film.[20,23–25] Pump-probe spectroscopy has confirmed a similar mechanism underlying the UV-induced decomposition of transition metal oxalate complexes.[26] A detailed understanding from the transition metal perspective is currently lacking. The blending of multiple transition metals together in precursor films,[21] for instance, is known to alter decomposition kinetics but an underlying reason for these changes is not established. Analysis of the mechanism from this perspective requires that the coordination environment be monitored as a function of photolysis time.

The identification of ligand coordination modes and analysis of their evolution during photolysis would provide useful mechanistic information. Carboxylates are common ligands that coordinate to transition metal ions through several distinct binding modes. Deacon and Phillips established the most widely utilized diagnosis criteria for carboxylate coordination modes using IR spectra from crystalline acetate and trifluoroacetate complexes.[27] They identified that the energy difference (Δ) between the symmetric carboxylate stretching frequency, ν_s, and the higher energy asymmetric stretching frequency, ν_{as}, were related to the coordination mode. Using this approach, a $\Delta > 200$ cm^{-1} was shown to indicate carboxylate ligands bound in a monodentate fashion, ligands bound in chelating fashion exhibit a lower Δ than the ionic species (typically < 150 cm^{-1}), and ligands bound in bridging mode lie in between.[27] Deacon and Phillips highlighted the empirical nature of their results and emphasized the risks in utilizing Δ to correlate carboxylate coordination geometry in complexes other than the acetates which they studied.[27] Subsequent research confirmed that the direction and magnitude of shift in ν_s and ν_{as} are ineffective at identifying binding modes,[28] but extensive citations of the original work attest to the validity and breadth of application of Δ to determine carboxylate binding modes. This approach has been used to assign the coordination motifs in the structural characterisation of self-assembled monolayers of *n*-alkanoic acids,[29] metal organic frameworks,[30,31] nanocomposites,[32] CO_2 adsorption,[33] polymers,[34,35] paints,[36] and proteins.[37] The FTIR spectra on the metal-organic precursors utilized here exhibit the typical problems of extensive overlapping absorbance bands in the ν_{as} region, due to co-existence of multiple coordination environments and δ_{CH} bands, which inhibits confident assignment using the Deacon and Phillips method. A means to assign absorbance bands with confidence is required.

Generalized two-dimensional correlational spectroscopy (2D-COS) was developed by Noda as a mathematical means to enable assignment of challenging spectra. 2D-COS relies on the acquisition of a series of spectra following the application of an external perturbation to a system.[38–42] A detailed description is provided in a biannual review.[42] The technique takes a reference spectrum for a series of *m* spectra, typically the average of all *m* spectra in the series, and uses it to calculate a *dynamic spectrum*:

$$\tilde{A}(\nu_k,\ s_i) = \begin{cases} A(\nu_k,\ s_i) - \bar{A}(\nu_k);\ for\ 1 \le i \le m \\ 0; otherwise \end{cases} \quad (1)$$

Where ν_k represents the spectral variable, s_i the perturbation variable, and $\bar{A}(\nu_k)$ is the reference spectrum. This dynamic spectrum can be used to calculate several useful types of 2-D spectra. A *synchronous spectrum* indicates the magnitude of change in absorbance at two arbitrary wavenumbers (numeric value) and whether absorbance is changing in the same (positive value) or opposite directions (negative value). The synchronous spectrum can be calculated as:

$$\Phi(\nu_1, \nu_2) = \frac{1}{m-1}\sum_{i=1}^{m} \tilde{A}(\nu_1,\ s_i).\tilde{A}(\nu_2,\ s_i) \quad (2)$$

A 2-D *disrelation spectrum* indicates whether changes in absorbance are synchronized with respect to the perturbation or not, with observation of cross peaks indicating a lack of synchronization. It is calculated as:

$$|\Lambda(\nu_1, \nu_2)| = \sqrt{\Phi(\nu_1, \nu_1).\Phi(\nu_2, \nu_2) - \Phi(\nu_1, \nu_2)^2} \quad (3)$$

Herein, we utilize 2D-COS to perform a detailed analysis of the photochemically induced decomposition of a series of 11 metal-organic complexes containing carboxylate ligands. We simultaneously demonstrate the utility of 2D-COS for tracking complex solid-state reactions to extract mechanistic information for this synthetic protocol, from the perspective of the transition metal centers. We show that the decomposition consistently involves an initial conversion of ligands from monodentate or bridging binding modes into chelating modes, which is followed by decomposition of ligands in this mode. Electronegativity is shown to be a dominant factor in determining reaction kinetics, with a second factor becoming important for transition metals with low electronegativity.

2. EXPERIMENTAL

2.1 Materials

Nickel(II) 2-ethylhexanoate (78% in 2-ethylhexanoic acid, 10-15% Ni), copper(II) 2-ethylhexanoate (solvent free, 16-19% Cu), iron(III) 2-ethylhexanoate (6% Fe in mineral spirits, 99.998+%-Fe), zinc(II) 2-ethylhexanoate (18% Zn in mineral spirits), manganese(II) 2-ethylhexanoate (40% solution in mineral spirits, 6% Mn), cobalt(II) 2-ethylhexanoate (12% Co in mineral spirits) and sodium 2-ethylhexanoate (60% in water) were used as received from Strem Chemicals. Fluorine-doped tin oxide glass (FTO; TEC-7 grade, Hartford Glass) was used as a substrate and was cleaned immediately prior to use by sequential ultrasonication in a detergent solution, milli-Q H_2O (18.2 MΩ), then isopropanol. The surface was dried under a stream of N_2 and placed in a custom UV-irradiation chamber (GHO18T5VH lamp, Atlantic Ultraviolet) for 15 minutes.

2.2 Film Fabrication

Ethanol-based solutions containing a total metal concentration of 0.3 M were prepared. Thin, solid films of the selected precursors were prepared by spin-coating the solutions on freshly cleaned FTO coated glass at 3000 rpm for 60 seconds. A series of 6 single transition metal films (Mn^{2+}, Fe^{3+}, Co^{2+}, Ni^{2+}, Cu^{2+}, Zn^{2+}) and five bimetallic films were by mixing 50:50 ratio of Ni^{2+} and M^{x+} (M^{x+} = Mn^{2+}, Fe^{3+}, Co^{2+}, Cu^{2+}, Zn^{2+}) were prepared in triplicate and irradiated under a UV lamp (Atlantic Ultraviolet, GHO18T5VH). The photochemical decomposition of each film was tracked by removing all samples from the photolysis chamber at prescribed times and acquiring infrared spectra.

2.3 Infrared Spectroscopy

FTIR spectroscopy was performed using a Nicolet 6700 equipped with a VeeMAX III sample stage (PIKE Technologies). Measurements were performed in reflection mode with an incident angle of 50 degrees, where the FTO reflects radiation in the region of interest. A new reference spectrum was obtained for each time interval using a blank FTO substrate. The mathematical processing required for the dynamic, synchronous, and disrelation spectra was carried out with equations (1) – (3) using the Numpy package (Version 1.19.2) for Python 3.7.

3. RESULTS AND DISCUSSION

3.1 FTIR of Monometallic Precursor Films

Thin films of six different transition metal complexes were deposited on FTO glass for systematic analysis of decomposition mechanisms. A spectrum of sodium 2-ethylhexanoate is representative of free, or “ionic”, ligands because sodium ions exhibit little bonding character.[43] Prominent features in this spectrum include a series of peaks between 2700-3000 cm^{-1}, a strong peak at 1550 cm^{-1}, a weak peak at 1459 cm^{-1} with a shoulder at 1446 cm^{-1}, and a moderate peak at 1415 cm^{-1} (Figure 1A). The peaks in the high-frequency region can be assigned to C-H stretching modes (ν_{CH}). An expected C-H bending mode (δ_{CH}) should be relatively weak and largely independent of the identity of the coordinating cation. The relative intensity and stability of the peaks at 1459 and 1446 cm^{-1} across all samples enables assignment to δ_{CH} vibrational modes (Figure 1A). The remaining peaks at 1550 and 1415 cm^{-1} in sodium 2-ethylhexanoate are assigned as the asymmetric (ν_{as}) and symmetric (ν_s) carboxylate stretching modes, respectively. An increased number of peaks in the fingerprint region for transition metal complexes reveals an oligomeric structure containing multiple binding modes (Figure 1A).

A composition-dependent change in the number and location of peaks is observed in the FTIR spectra. The region from *ca*. 1500 to 1720 cm^{-1} exhibits a change in both the number and location of peaks as the transition metal is varied. The iron sample is the most convoluted spectrum for single transition metal complexes, with four major component peaks in this region, while the single major peak in the copper sample makes it the simplest (Figure 1A). The lower frequency ν_s mode is observed as a single feature located between 1400 and 1427 cm^{-1} across the composition series (Figure 1A, Table S1). This feature tends to broaden and gain asymmetry as the number of ν_{as} peaks present in the spectrum increases, suggesting that multiple unresolvable peaks may contribute to the feature. This behavior is in agreement with the literature, where a compilation of 63 transition metal carboxylate complexes show an average ν_s location of 1422 ± 19 cm^{-1}.[27,28] Bonding interactions between the carboxylate motif and the transition metal centers thus vary as a function of element and coordination geometry, enabling changes in coordination modes to be tracked by monitoring ν_{as} and ν_s.

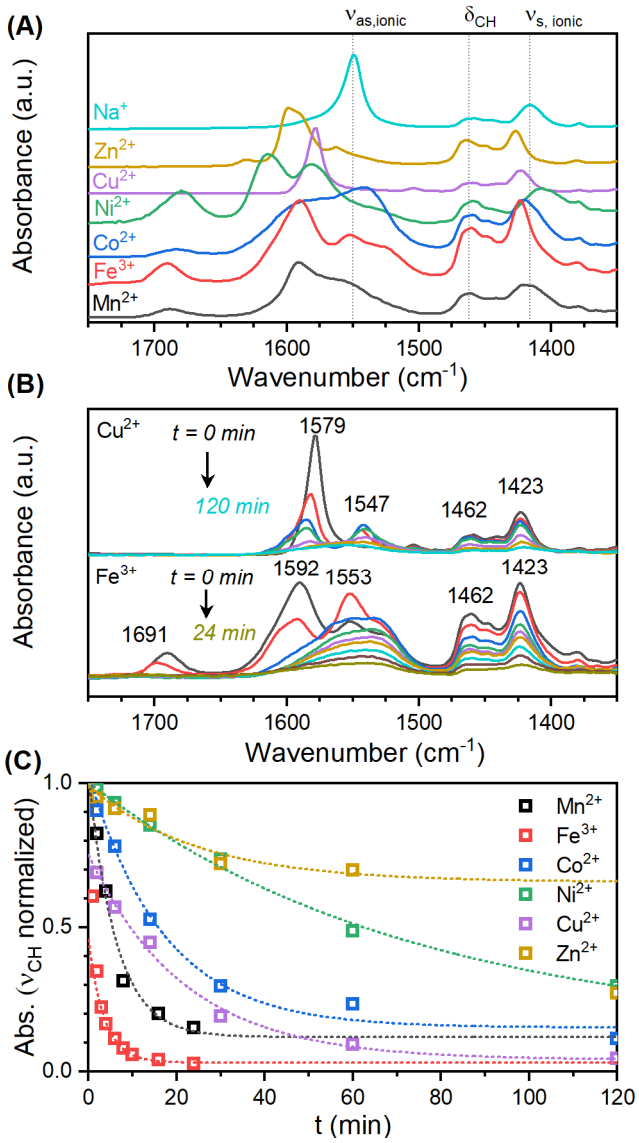

Figure 1. Infrared spectra for the monometallic metal 2-ethylhexanoate complexes. **(A)** Fingerprint region containing the C-H bending vibration (δ_{CH}) and the symmetric (ν_s) and asymmetric (ν_{as}) carboxylate stretching vibrations. **(B)** Change in FTIR spectra as a function of UV irradiation time for Cu(II) 2-ethylhexanoate (upper traces) and Fe(III) 2-ethylhexanoate (lower traces). **(C)** First-order exponential decay kinetics for normalized ν_{CH} vibrations with irradiation time.

Carboxylate ligands can bind transition metals in κ^1- (monodentate), κ^2- (bidentate chelating), and μ^2- (bidentate bridging) modes (Scheme 1). All samples show a blend of the three coordination motifs, with a fourth peak is observed near 1550 cm^{-1} clearly visible in some samples that is assigned as free ligand based on alignment with the sodium sample. The monometallic samples show a peak that is higher in energy than the free ionic ligand, but lower than expected for monodentate coordination. This peak can be assigned to ligands in a

bridging coordination environment (Figure 1A). Confident assignment of bridging and chelating modes can be accomplished when all four possible carboxylate motifs are observed, as in the iron sample, so that they can be directly compared to one another. Assignment is much more ambiguous for the remaining samples, however, because transition metal variation induces peak shifts on the order of 100 cm^{-1}. Confident assignment of vibrational modes in all samples is therefore best made after an extra dimension of information has been added to the data (*vide infra*).

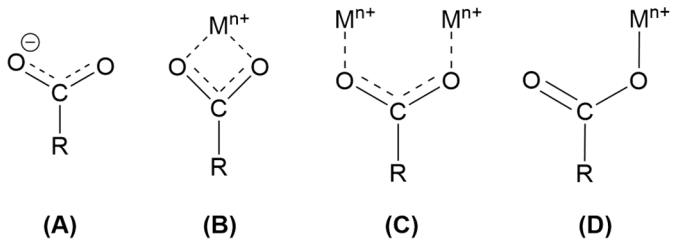

Scheme 1. Binding geometries present in transition metal carboxylate precursor films. Ionic **(A)**, bidentate chelate **(B)**, bidentate bridging **(C)**, and monodentate **(D)** binding motifs.

3.2 Photochemical Decomposition of Monometallic Precursors

The behavior of vibrations from the organic ligands during photo-induced decomposition provides insights into the underlying structural evolution and reaction mechanism.[20,23,24] A continual decrease in the intensity of ν_{CH} and δ_{CH} bands with time exposed to UV irradiation signifies a loss of ligands from the film (Figures 1B and S1). This ligand loss process has been documented, with GC-MS studies indicating a mechanism whereby a ligand-to-metal charge transfer reaction is followed by a series of radical reactions to liberate CO_2 and gaseous hydrocarbons.[17,18,23,24,44] Following an initial induction period an exponential decay of C-H absorbance bands is observed with time, indicating ligands are lost through a first order reaction mechanism for all samples (Figure 1C). The observed rate constant (k_{obs}) for ligand loss is dependent on transition metal identity (Table 1). The induction period at early stages of decomposition deviates from this exponential trajectory, with Fe, Mn, Co, and Cu samples decaying faster than expected, but Ni and Zn more slowly. The ν_s peak behavior is similar to the C-H vibrations, but pronounced changes are observed in the ν_{as} region during the early stages of decomposition. In this region, the Fe and Cu samples show complete decay of the two highest energy peaks with simultaneous growth of a peak in the low energy portion of the ν_{as} region

(Figure 1B). The remaining monometallic samples show continual but uneven decomposition, with the higher energy peaks decaying faster than the low energy peaks (Figures S2, S3). These observations indicate that the ligand-binding mode plays an important role in the decomposition mechanism.

Table 1. Observed rate constants for photochemically induced decomposition for monometallic transition metal complexes and 1:1 bimetallic mixtures.

Composition	k_{obs} (min^{-1})	Composition	k_{obs} (min^{-1})
Mn^{2+}	0.186 ± 0.012	$Ni^{2+}Mn^{2+}$	0.101 ± 0.007
Fe^{3+}	0.272 ± 0.025	$Ni^{2+}Fe^{3+}$	0.128 ± 0.010
Co^{2+}	0.064 ± 0.005	$Ni^{2+}Co^{2+}$	0.026 ± 0.002
Ni^{2+}	0.021 ± 0.002	$Ni^{2+}Cu^{2+}$	0.042 ± 0.002
Cu^{2+}	0.047 ± 0.003	$Ni^{2+}Zn^{2+}$	-
Zn^{2+}	0.009 ± 0.002	$Ni^{2+}Sn^{2+}$	0.014 ± 0.001

3.3 Correlational Analysis of Monometallic Films

The time-dependent data provides an extra dimension of information that enables 2-D correlational analysis to isolate and confidently assign individual absorbance bands, and to study the interconversion of specific coordination modes. Correlational analysis is split into two plots. The synchronous 2D-COS spectrum enumerates the extent of simultaneous change of absorbance at arbitrary energies, ν_1 and ν_2. It is always symmetric, with autopeaks appearing on the diagonal (i.e., when $\nu_1 = \nu_2$), but cross peaks can be either positive or negative. Positive cross peaks signify a shared increase or decrease in signal over the selected perturbation period, while a negative sign indicates an increase in one and a decrease in the other. The disrelation component of 2D-COS contains no autopeaks and is always antisymmetric, with the sign of cross peaks inverted across the diagonal. Observed cross peaks represent a lack of synchronization in changes in spectral intensity, regardless of direction (i.e., ν_1 can be decreasing while ν_2 is either increasing or decreasing simultaneously). 2D-COS data is available for all monometallic samples (Figures 2, S4-S7); Cu and Fe samples represent the simplest and the most complex case, respectively, and will serve as the center of discussion. Because all peaks exhibit complete decay over the experimental timeframes, correlational analysis across each complete data series would result in convolution of multiple distinct reaction steps. Resolution of the induction process is achieved by analyzing each dataset split into two distinct time regions, where the second time region is defined as starting where clear and consistent exponential decay begins.

The Cu sample is useful for initial exploration of 2D-COS due to its well-resolved peaks and straightforward behavior. The early stage of decay in the copper sample involves the loss of one carboxylate coordination mode and the gain of an alternative one, as evidenced by decreased intensity of a ν_{as} peak at 1578 cm^{-1} and simultaneous appearance and growth of a peak at 1542 cm^{-1} (Figure 1B). This is followed by simultaneous decay of both modes as photolysis time progresses, with a broad product-based absorbance band growing in around 1560 cm^{-1}. The synchronous plot for the early stage of decomposition shows that the ν_{as} at 1578 cm^{-1} has positive correlations with the ν_s at 1423 cm^{-1}, but strong negative correlations with the peak at 1542 cm^{-1} (Figure 2A). The disrelation plots in this timeframe are indistinguishable from noise levels (Figure 2B). Together, these plots indicate that the decay and growth of these two ν_{as} peaks are concerted – the species responsible for the high energy ν_{as} is converted into that responsible for the lower energy ν_{as}. The simultaneous loss of ligands from both binding modes during the second time region is seen as positive cross peaks for all spectroscopic features in the synchronous spectrum (Figure 2C). The disrelation plot provides clear evidence that peak decay is not universally synchronized (Figure 2D). The multi-component autopeak that straddles the diagonal line near 1587 cm^{-1} is due to the peak shift to higher energy with irradiation time. The splitting of the autopeak near 1542 cm^{-1} captures the change in peak shape, which is induced by the growth of a broad absorbance band from the product. The 1587 cm^{-1} feature shows strong negative (horizontal axis) cross peaks with all other features, signifying that it is lost before the other features. The lower energy ν_{as} peak shows minor cross peaks with the δ_{CH} and ν_s peaks, with positive cross peaks surrounding it due to growth in the product absorbance. A mechanism consisting of at least two major steps is therefore required to describe decomposition for the Cu precursor. The initial coordination mode must be converted into an intermediate coordination mode before the complex can proceed with loss of ligands.

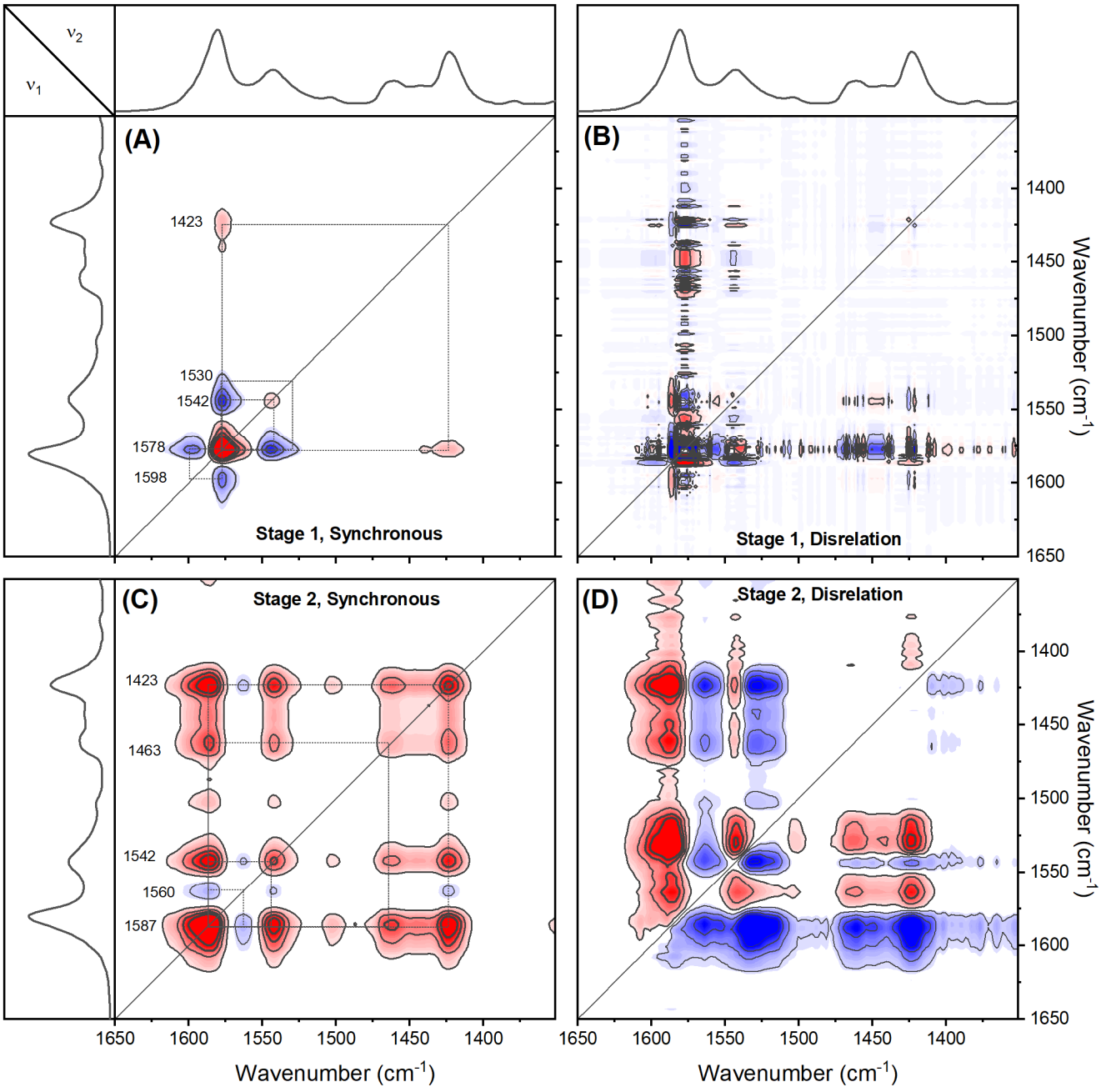

Figure 2. Two-dimensional correlation IR spectroscopy for photochemically induced decomposition of copper(II) 2-ethylhexanoate. **(A)** Synchronous and **(B)** disrelation plots in the first stage of decomposition. **(C)** Synchronous and **(D)** disrelation plots in the second stage of decomposition. Reference spectra shown along the edges is the average of all spectra across the time series.

The correlational data for decomposition of the Fe complex is considerably more complex, with at least four overlapping peaks initially present in the ν_{as} region, with each showing varied

growth and decay. The first stage of decay, from 0 to 2 minutes, shows prominent autopeaks at 1589 and 1552 cm^{-1} (Figure 3A). These features are both asymmetric, with the 1589 cm^{-1} peak smearing to higher energy due to a peak shift, and the 1552 cm^{-1} smearing to lower energy due to initial growth and then persistence of intensity at 1531 cm^{-1}. The peak at 1589 cm^{-1} is positively correlated to all features except that between 1552-1531 cm^{-1}, which itself is negatively correlated to all other features. The disrelation plot reveals only background noise in this region (Figure 3B). These correlations indicate that the initial stage of decomposition involves synchronized removal of carboxylate ligands from two distinct coordination environments, with these carboxylate ligands being transferred into either one or two new carboxylate environments. Synchronous plots for the second stage of decay show continuous loss of all remaining features, with a broad and asymmetric feature between 1552-1531 cm^{-1} suggesting co-existence of two peaks in this area (Figure 3C). The cross peaks between the ν_{as} and ν_{s} regions of the disrelation plots for this region (Figure 3D) indicate asynchronous loss, which supports the assessment that two major features exist at 1552 and 1531 cm^{-1}. Further support for the co-existence of two peaks is provided by the growth of a strong and well-defined peak at 1552 cm^{-1} in the early stages of decomposition (Figure 1B). The decomposition reaction is thus initiated by conversion of the two coordination modes responsible for ν_{as} signals at 1686 and 1589 cm^{-1} into those at 1552 and 1531 cm^{-1}. This is followed by simultaneous decay of the ν_{as} signals at 1552 and 1531 cm^{-1}. Correlational analysis shows that the Mn, Co, Ni, and Zn precursor films all show a two-step decay process similar to those described above (Figures S4-S8), albeit over different time regions and a different relative distribution of individual ν_{as} modes.

The observation of consistent behavior across the series of transition metal complexes enables confident assignment of ν_{as} vibrational bands to specific coordination motifs. The ν_{s} vibrational mode exhibits only a single cross peak to all ν_{as} bands for each sample, which is due to the smaller shift in location of this peak as discussed above. This makes it impossible to directly assign ν_{s} to specific carboxylate motifs, but facilitates assignment of the ν_{as} bands by providing a single anchor point to determine Δ. The spacing between cross peaks in the synchronous correlation plots provides a convenient and consistent method to extract Δ for overlapping peaks (Table S2). All Δ values observed for each sample in the series can be classified into one of four sets (Figure 4A). Literature precedence leads us to use Δ values to

assign individual ν_{as} vibrations to 2-ethylhexanoate ions with monodentate (Δ = 258-300 cm^{-1}), bridging (Δ = 150-212 cm^{-1}) or chelating (Δ <135 cm^{-1}) binding modes; the presence of a peak near 1550 cm^{-1} provides a Δ of *ca*. 135 cm^{-1} that is indicative of free ligands (Figure 1).[27]

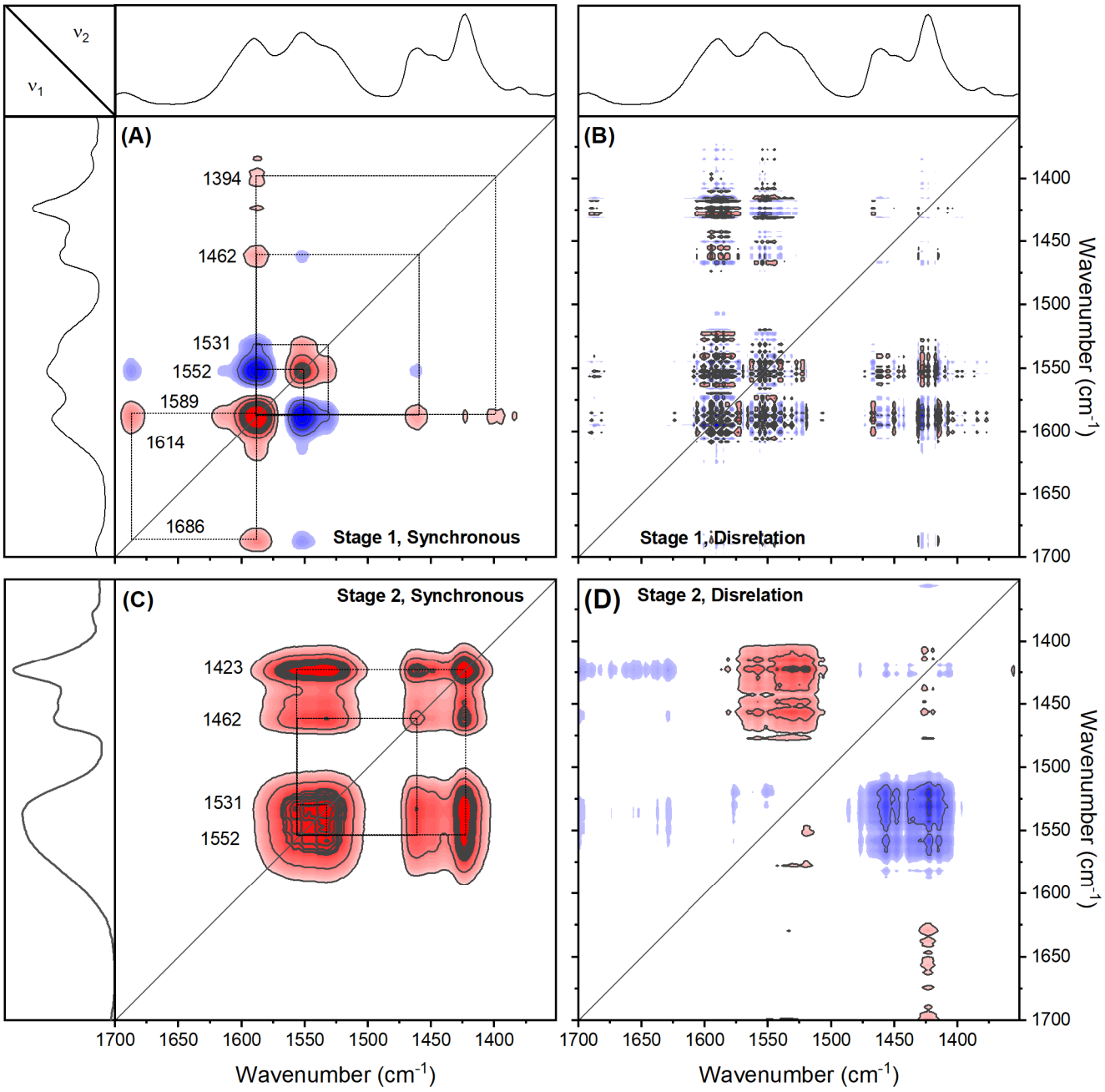

Figure 3. Two-dimensional correlation spectroscopy for photochemically induced decomposition of iron(III) 2-ethylhexanoate. **(A)** Synchronous and **(B)** disrelation plots in the first stage of decomposition. **(C)** Synchronous and **(D)** disrelation plots in the second stage of decomposition. Reference spectra shown along the edges is the average of all spectra across the time series.

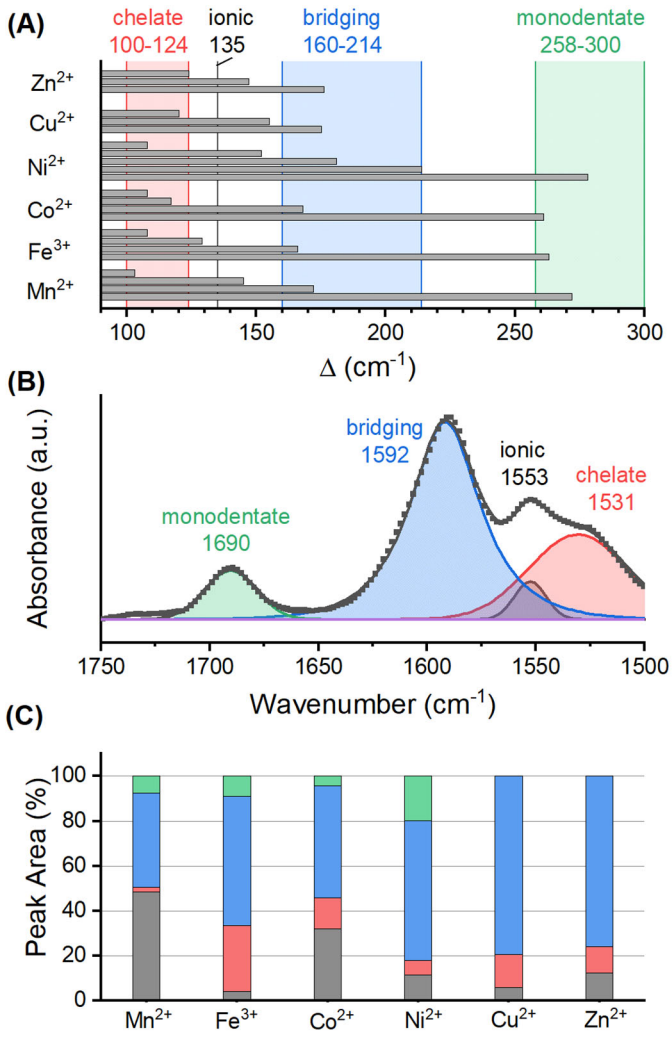

Figure 4. Diagnosis of binding motifs via FTIR spectroscopy. **(A)** The differences between asymmetric and symmetric carboxylate stretching frequencies for monometallic precursor films; obtained from synchronous 2D IR spectra. **(B)** Component peaks for the pristine iron 2-ethylhexanoate film. **(C)** Percentage of total peak area captured by each binding motif for pristine monometallic precursor films. Curve fits were performed on the spectra in Figure 1A.

The assignment of ν_{as} peaks to specific ligand environments enables approximation of the relative amount of ligand in each environment. A curve-fitting protocol was used, with the location of component peaks restricted to ranges with Δ values described above. The area of the component peaks from fitting results (Figures 4B, S9) provides a measure of the relative amount of the four possible environments for 2-ethylhexanoate in each solid-state precursor film (Figure 4C). The majority of ligands are bound in bridging motifs for all precursor

complexes, with a substantial amount of chelation observed only for Fe and Co. No discernible trend is observed for the distribution of binding modes in the series.

3.4 FTIR of Bimetallic Precursor Films

Analysis of a series of mixed metal precursor films where Ni is blended with other transition metals in a 1:1 ratio provides insight into the changes in decomposition kinetics. These mixed metal films are qualitatively like the monometallic precursors, with each spectrum possessing a single ν_s peak but multiple ν_{as} peaks (Figure 5A). A two-stage decay is prominent in the lowest energy ν_{as} peak for all but the Ni-Zn composition, which exhibited negligible decay over time (Figure S10). The first stage involves the loss of bridging and monodentate ν_{as} peaks and simultaneous growth in the chelate peak, which is readily observed in plots of absorbance against photolysis time for these features (Figure 5B-C). The second stage of decay can once again be fitted with a single exponential, indicating a mechanism that is first order with respect to the chelating ligands. The k_{obs} extracted from each of the binary mixtures for this second stage of decay is increased relative to the Ni precursor alone, with the effect most pronounced for the Fe-Ni and Mn-Ni mixtures (Table 1, Figures 5D, S11). The energy region where the bridging ν_{as} appears splits into multiple distinguishable features, which was not observed for any of the monometallic samples. This splitting of ν_{as} peaks likely reflects the participation of two different transition metal ions in the bridging motif. The uniformity of decay despite the greater complexity of the spectra suggests that transition metal ions are homogeneously distributed in the films. This initial transfer of carboxylate ligands into chelating environments thus appears to be a necessity for photochemical decomposition.

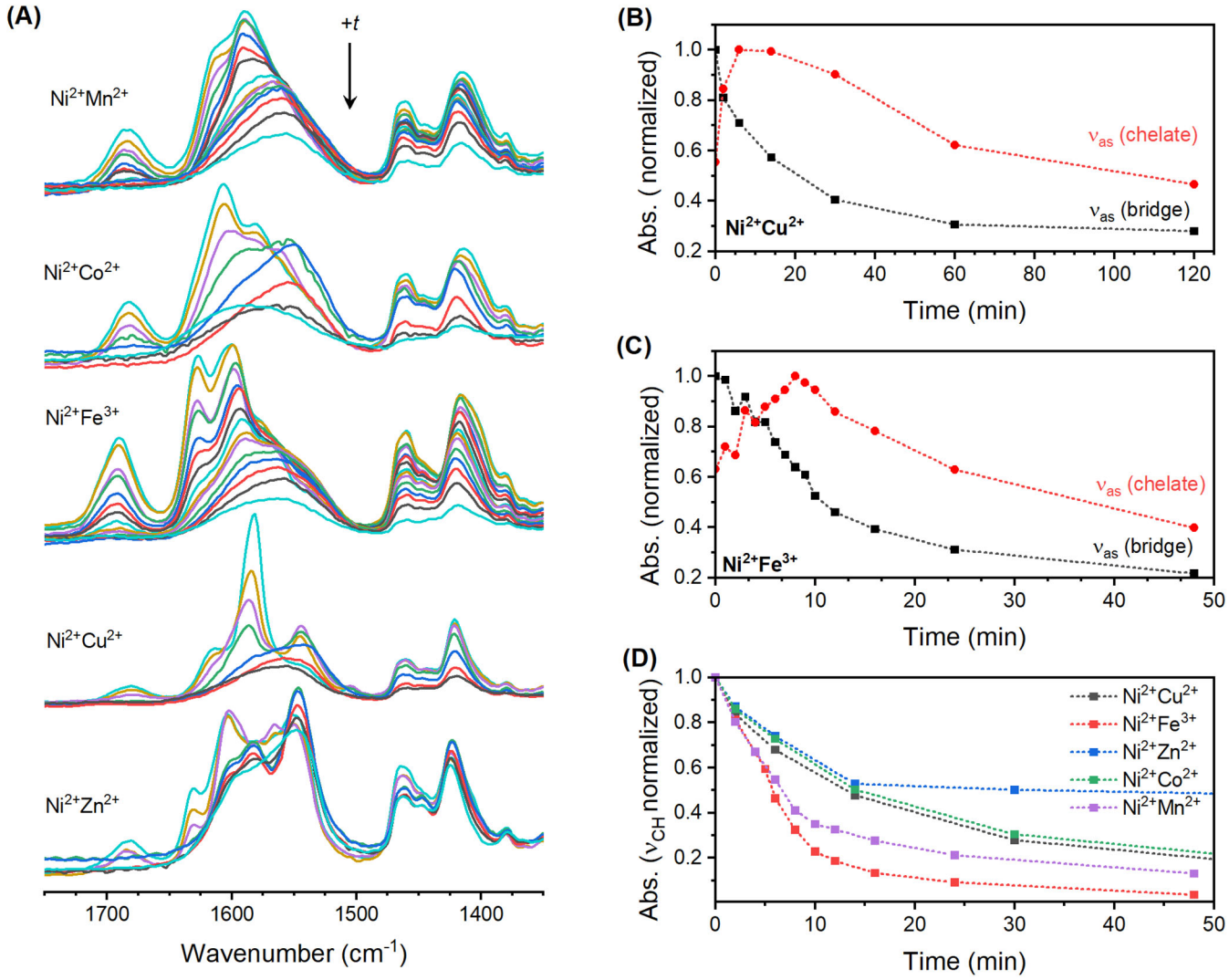

Figure 5. Infrared spectra for films with a 1:1 stoichiometric mixing of transition metals. **(A)** Transformation of the fingerprint region following irradiation with UV light. A comparison of changes in the chelating and bridging motifs is provided for **(B)** Ni-Cu and **(C)** Ni-Fe samples. **(D)** A comparison of the rate of ligand loss, as judged by ν_{CH}, for all films with binary compositions.

3.5 Correlational Analysis of Bimetallic Films

Direct comparison of the 2-D correlational spectroscopy results for the Ni sample and the Fe-Ni sample confirms changes in location of individual vibrational bands, but preservation of the overall mechanism (Figure 6). The synchronous correlation plots once again resolve overlapping peaks and identify prominent Δ values, with a total of 6 peaks across the Fe-Ni ν_{as} region. Based on the regions defined above, these peaks can be assigned to one

monodentate motif (1689 cm^{-1}), three bridging motifs (1627, 1606, and 1577 cm^{-1}), and two chelating motifs (1546 and 1533 cm^{-1}). The highest and lowest energy peaks observed in the region for bridging motifs can be assigned to Ni-Ni and Fe-Fe bridging modes based on their proximity to those for monometallic Ni (1618 cm^{-1}) and Fe (1590 cm^{-1}), leaving the central peak to be assigned as a Ni-Fe bridged motif. The two peaks for ν_{as} chelating motifs in the mixed metal films show excellent agreement with those for the monometallic nickel (1544 cm^{-1}) and iron (1531 cm^{-1}) films, allowing their direct assignment. The observed splitting of ν_{as} peaks in the binary films thus arises due to the existence of three possible bridging motifs in a binary mixture (Ni-Ni, Ni-M, M-M), and two possible chelating motifs (Ni and M). The signs of correlations in the synchronous plot indicate that the first stage of decomposition again involves a transition of all monodentate and bridging ligands into chelating geometries (Figures 6A and 6C), with all remaining features decaying during the second stage (Figure S12). Disrelation plots for the binary samples are complex (Figure 6D), but the lack of a cross peak between 1531 and 1461 or 1403 cm^{-1} stands out. This lack of a peak indicates synchronized changes in signal intensity at these energies. Since the 1461 and 1403 cm^{-1} peaks capture the entirety of ligands in the system, this implies that the majority of ligands lost from the system decompose through a chelated Fe center. These combined results indicate that although the number of resolvable ν_{as} peaks and their locations changes as a function of film composition, consistency in the decomposition mechanism exists across all samples analyzed here. The consistency of a single mechanism (Figures S13-S16), but changes in k_{obs} relative to the monometallic samples (Table 1) indicates that the decomposition reaction is tuned either by influencing the rate of transition to chelating motifs or by increasing the rate of decomposition of carboxylate in chelating environments.

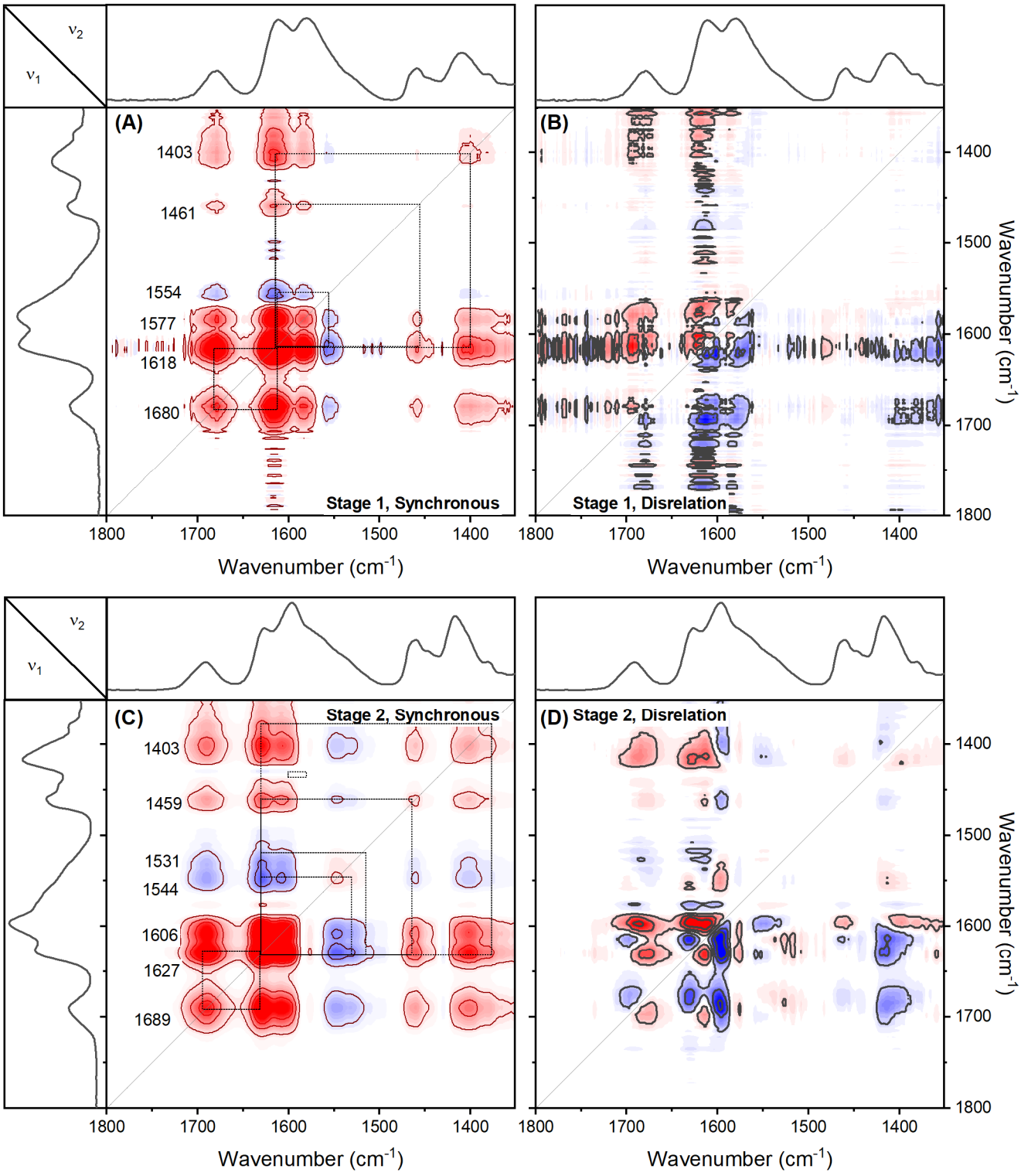

Figure 6. Comparison of two-dimensional correlation spectroscopy for photochemically induced decomposition of a pure Ni(II) film with a 1:1 mixture of Fe(III) and Ni(II). **(A)** Synchronous and **(B)** disrelation plots in the first stage of decomposition of the Ni sample. **(C)** Synchronous and **(D)** disrelation plots in the first stage of decomposition for the Fe-Ni sample.

3.6 Property Trends

The electronegativity and pK_a of hexaaqua metal ions of the transition metals were the only properties inspected that showed clear correlations with decomposition reaction kinetics. Plots of experimentally determined pK_a values for hexaqua-metal complexes against k_{obs} exhibit a distinctive V-shape, with the trend spanning both monometallic and bimetallic composition (Figure 7A; pK_a values in bimetallic taken as the average of the two transition metals). This correlation carries over to plots of k_{obs} versus electronegativity (Figure 7B), as expected because each parameter provides a measure of Lewis acidity of the transition metal centers.[45–47] Additional properties explored include hydration enthalpy, d-electron count, and relative percentage of each carboxylate binding mode, but each showed no clear correlations with k_{obs} (Figures S17, S18). The location of ν_{as} for the monodentate carboxylate motif shows similar trends when plotted against pK_a and electronegativity (Table S3, Figure S19), which leads to a positive linear correlation between k_{obs} and ν_{as} of the monodentate carboxylate binding motif (Figure 7C).

3.7 Mechanistic Implications

The spreading of spectroscopic information over a time dimension enables 2D-COS to identify structural details for the transition metal centers and track their evolution during the decomposition reaction. Assignment of individual absorbance bands to ligands in monometallic, bridging, and chelating coordination environments enables the time series data to be analyzed through a combination of synchronicity in direction of change in absorbance (synchronous cross peak sign) and time (disrelation spectra). This analysis clearly depicts a two-stage reaction, where the first stage is an induction period that is dependent on the relative proportion of each binding mode present in the precursor. The negative cross peaks and synchronicity between ν_{as} (bridge) and ν_{as} (chelate) during the early stage of decay (Figures 2, 3) provides evidence for the conversion into chelating environments. Comparisons of absorbance bands for ν_{CH} or δ_{CH} with ν_{as} (chelate) and ν_{as} (bridge) confirm the existence of the two decay stages and suggest that the second stage is primarily the loss of chelating motifs (Figure 5). This second region is characterized by an exponential decay that is indicative of a first order reaction with respect to the chelate motif.

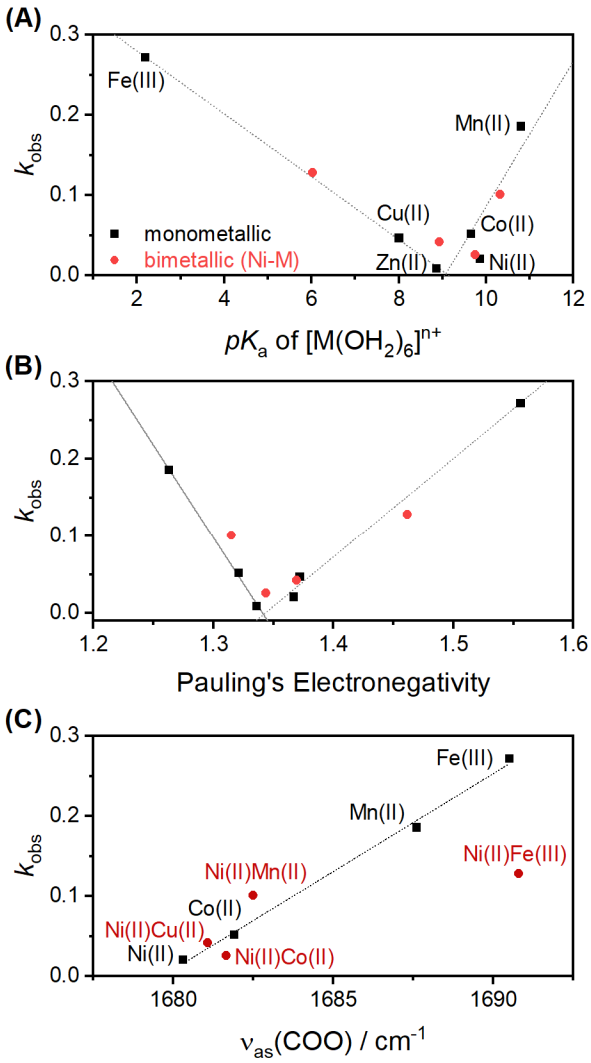

Figure 7. Correlations observed for decomposition rate. The measured k_{obs} yields a V-shaped correlation against **(A)** pK_a of aqua metal ion and **(B)** Pauling's electronegativity. **(C)** A linear correlation is found for k_{obs} versus ν_{as} for monodentate coordination motif.

The bimetallic precursor films exhibit increased complexity in their spectra, but the decomposition pathway is consistent with that of the monometallic films. The monometallic films exhibit a single absorbance band for each of the three coordination motifs, but the bimetallic compositions show a combination of monodentate, three bridging, and two chelating motifs. Despite this increased complexity, the bimetallic films continue to exhibit two stage decay. The first order rate constant extracted from the second stage of decay falls in between those of the two components, suggesting concerted decay rather than individual decay of the two components. This attests to the homogeneity of both the precursors and the resultant metal

hydroxide films. The Sabatier Principle predicts a “volcano” plot when a material property such as electronegativity is tuned.[48] The observation of a less-conventional V-shaped correlation between pK_a (or electronegativity) and k_{obs} (Figures 7A, 7B) therefore reveals the co-existence of two factors that influence reaction rate. One possibility is a change in mechanism from M-O bond cleavage at low electronegativities to C-O cleavage at high electronegativities. Although monodentate ligands are not involved in the final decay of the complexes, the positive correlation between ν_{as} for monodentate ligands in the precursor and k_{obs} (Figure 7C) reveals the importance of M-O bond strength. A blue shift in vibrational frequency signifies stronger C=O bonds in this coordination motif. A stronger M-O bond would make the second oxygen more electron deficient, thereby inducing this blue shift. We propose that strengthening of M-O bonds alters the mechanism to facilitate direct cleavage of the C-O single bond. The protonation state of the oxide ligands on the metal also appears critical, with the minimum k_{obs} occurring at a hexaaqua transition metal pK_a close to the pK_b (9.18) for 2-ethylhexanoate. The ν_{OH} region of the IR spectra contains a broad band for all samples, but a much narrower peak at ca. 3590 cm^{-1} for Ni, Co, Ni-Zn, and Ni-Co, all of which lie near this pK_b value (Figure S11). The presence of aqua, hydroxo, and oxo ligands in the precursor material may therefore play a key role in tuning the reaction rate. Regardless of the underlying reasons, the previously established mechanisms for photochemically induced decomposition of metal carboxylate complexes can be refined to include the specific structural changes for the transition metal coordination environment (Scheme 2).[27,49]

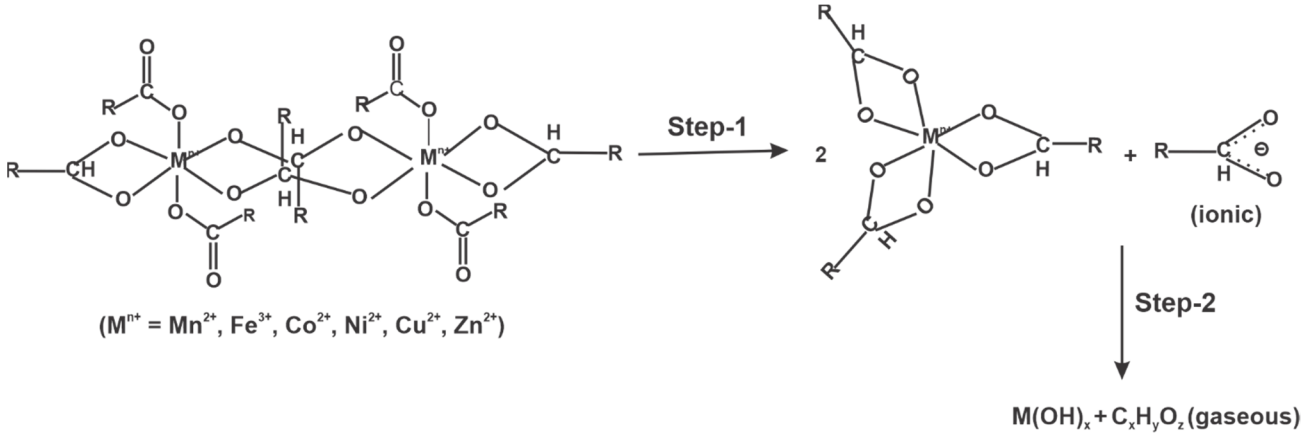

Scheme 2. Proposed mechanism in the photochemical decomposition of transition metal carboxylates.

CONCLUSIONS

Two-dimensional infrared correlation spectroscopy was demonstrated to be a powerful tool for extracting mechanistic information for solid-state reaction mechanisms. The photochemically induced conversion of thin films of transition metal 2-ethylhexanoate complexes into metal oxides was studied for a series of 11 metal-organic complexes, where the infrared spectra of the ligands provide an effective means to monitor the reaction progress. The synchronous component of 2D-COS spectra enabled confident assignment of absorbance bands to ligands bound in a chelating, bridging, or monodentate fashion for even the most complex spectra, where 6 overlapping peaks were observed. The disrelation component of 2D-COS spectra indicates a two-stage decomposition for all monometallic and bimetallic samples due to the need to convert of bridging and monodentate ligands into chelating ligands before decomposition can proceed. A V-shaped correlation between the pK_a of hexaaqua metal ions (or electronegativity) and observed rate constant indicates that at least two competing factors control reaction rates. The importance of protons in the reaction is revealed by a minimum in V-shaped correlation at the pK_b of the carboxylate ligand, and by the presence of ν_{OH} vibrations for samples near the minimum. Metal-oxygen bond strength is identified as a second important consideration, with a linear correlation between carboxylate stretching frequencies and rate constant observed. These results advance the current understanding of photochemical decomposition of transition metal carboxylate complexes, demonstrate a means to identify and assign carboxylate coordination motifs in complex spectra, and demonstrate the utility of this simple-yet-powerful approach to extracting information from standard spectra.

ASSOCIATED CONTENT

Supporting Information. Tabulated FTIR peak locations, comprehensive FTIR spectra for photolysis times, 2D-COS spectra for all samples, kinetic traces, peak fits, and correlations between electronegativity and peak location. This material is available free of charge via the Internet at http://pubs.acs.org.

AUTHOR INFORMATION

Corresponding Author. rodsmith@uwaterloo.ca

Present Address. Department of Chemistry, University of Waterloo, 200 University Avenue W., Waterloo, Ontario, Canada N2L 3G1

Author Contributions. The manuscript was written through the contributions of all authors.

ACKNOWLEDGEMENTS

We thank the Natural Sciences and Engineering Research Council (NSERC) for funding through the Discovery Grants program.

REFERENCES

(1) Smith, R. D. L.; Pasquini, C.; Loos, S.; Chernev, P.; Klingan, K.; Kubella, P.; Mohammadi, M. R.; González-Flores, D.; Dau, H. Geometric Distortions in Nickel (Oxy)Hydroxide Electrocatalysts by Redox Inactive Iron Ions. *Energy Environ. Sci* **2018**, *11*, 2476–2485. https://doi.org/10.1039/C8EE01063C.

(2) Görlin, M.; Chernev, P.; De Araújo, J. F.; Reier, T.; Dresp, S.; Paul, B.; Krähnert, R.; Dau, H.; Strasser, P. Oxygen Evolution Reaction Dynamics, Faradaic Charge Efficiency, and the Active Metal Redox States of Ni-Fe Oxide Water Splitting Electrocatalysts. *J. Am. Chem. Soc.* **2016**, *138* (17), 5603–5614. https://doi.org/10.1021/jacs.6b00332.

(3) Friebel, D.; Louie, M. W.; Bajdich, M.; Sanwald, K. E.; Cai, Y.; Wise, A. M.; Cheng, M. J.; Sokaras, D.; Weng, T. C.; Alonso-Mori, R.; Davis, R. C.; Bargar, J. R.; Nørskov, J. K.; Nilsson, A.; Bell, A. T. Identification of Highly Active Fe Sites in (Ni,Fe)OOH for Electrocatalytic Water Splitting. *J. Am. Chem. Soc.* **2015**, *137* (3), 1305–1313. https://doi.org/10.1021/ja511559d.

(4) Trotochaud, L.; L. Young, S.; K. Ranney, J.; W. Boettcher, S. Nickel–Iron Oxyhydroxide

Oxygen-Evolution Electrocatalysts: The Role of Intentional and Incidental Iron Incorporation. *J. Am. Chem. Soc.* **2014**, *136* (18), 6744–6753. https://doi.org/10.1021/ja502379c.

(5) Burke, M. S.; Kast, M. G.; Trotochaud, L.; Smith, A. M.; Boettcher, S. W. Cobalt–Iron (Oxy)Hydroxide Oxygen Evolution Electrocatalysts: The Role of Structure and Composition on Activity, Stability, and Mechanism. *J. Am. Chem. Soc.* **2015**, *137* (10), 3638–3648. https://doi.org/10.1021/jacs.5b00281.

(6) Louie, M. W.; Bell, A. T. An Investigation of Thin-Film Ni–Fe Oxide Catalysts for the Electrochemical Evolution of Oxygen. *J. Am. Chem. Soc.* **2013**, *135* (33), 12329–12337. https://doi.org/10.1021/ja405351s.

(7) Kanan, M. W.; Nocera, D. G. In Situ Formation of an Oxygen-Evolving Catalyst in Neutral Water Containing Phosphate and Co^{2+}. *Science (80-.).* **2008**, *321* (5892), 1072–1075. https://doi.org/10.1126/science.1162018.

(8) Li, N.; Bediako, D. K.; Hadt, R. G.; Hayes, D.; Kempa, T. J.; von Cube, F.; Bell, D. C.; Chen, L. X.; Nocera, D. G. Influence of Iron Doping on Tetravalent Nickel Content in Catalytic Oxygen Evolving Films. *Proc. Natl. Acad. Sci.* **2017**, *114* (7), 1486–1491. https://doi.org/10.1073/pnas.1620787114.

(9) Trotochaud, L.; Ranney, J. K.; Williams, K. N.; Boettcher, S. W. Solution-Cast Metal Oxide Thin Film Electrocatalysts for Oxygen Evolution. *J. Am. Chem. Soc.* **2012**, *134* (41), 17253–17261. https://doi.org/10.1021/ja307507a.

(10) Klaus, S.; Louie, M. W.; Trotochaud, L.; Bell, A. T. Role of Catalyst Preparation on the Electrocatalytic Activity of $Ni_{1-x}Fe_xOOH$ for the Oxygen Evolution Reaction. *J. Phys. Chem. C* **2015**, *119* (32), 18303–18316. https://doi.org/10.1021/acs.jpcc.5b04776.

(11) Hunter, B. M.; Hieringer, W.; Winkler, J. R.; Gray, H. B.; Müller, A. M. Effect of Interlayer Anions on [NiFe]-LDH Nanosheet Water Oxidation Activity. *Energy Environ. Sci.* **2016**, *9* (5), 1734–1743. https://doi.org/10.1039/C6EE00377J.

(12) Blakemore, J. D.; Gray, H. B.; Winkler, J. R.; Müller, A. M. Co_3O_4 Nanoparticle Water-Oxidation Catalysts Made by Pulsed-Laser Ablation in Liquids. *ACS Catal.* **2013**, *3* (11), 2497–2500. https://doi.org/10.1021/cs400639b.

(13) Song, F.; Hu, X. Exfoliation of Layered Double Hydroxides for Enhanced Oxygen Evolution Catalysis. *Nat. Commun.* **2014**, *5* (1), 4477. https://doi.org/10.1038/ncomms5477.

(14) Yu, J.; Liu, J.; Clearfield, A.; Sims, J. E.; Speiegle, M. T.; Suib, S. L.; Sun, L. Synthesis of Layered Double Hydroxide Single-Layer Nanosheets in Formamide. *Inorg. Chem.* **2016**, *55* (22), 12036–12041. https://doi.org/10.1021/acs.inorgchem.6b02203.

(15) Smith, R. D. L.; Prévot, M. S.; Fagan, R. D.; Zhang, Z.; Sedach, P. A.; Siu, M. K. J.; Trudel, S.; Berlinguette, C. P. Photochemical Route for Accessing Amorphous Metal Oxide Materials for Water Oxidation Catalysis. *Science (80-.).* **2013**, *340* (6128), 60–63. https://doi.org/10.1126/science.1233638.

(16) Uppuluri, R.; Sen Gupta, A.; Rosas, A. S.; Mallouk, T. E. Soft Chemistry of Ion-Exchangeable Layered Metal Oxides. *Chem. Soc. Rev.* **2018**, *47* (7), 2401–2430. https://doi.org/10.1039/C7CS00290D.

(17) Avey, A. A.; Hill, R. H. Solid State Photochemistry of $Cu_2(OH_2)_2(O_2C(CH_2)_4CH_3)_4$ in Thin Films: The Photochemical Formation of High-Quality Films of Copper and Copper(I) Oxide. Demonstration Of. *J. Am. Chem. Soc.* **1996**, *118* (1), 237–238. https://doi.org/10.1021/ja952937j.

(18) Zhu, H. J.; Hill, R. H. The Photochemical Metal Organic Deposition of Manganese Oxide Films from Films of Manganese(II) 2-Ethylhexanoate: A Mechanistic Study. *J. Non. Cryst. Solids* **2002**, *311* (2), 174–184. https://doi.org/https://doi.org/10.1016/S0022-3093(02)01369-8.

(19) Mishra, S.; Daniele, S.; Hubert-Pfalzgraf, L. G. Metal 2-Ethylhexanoates and Related Compounds as Useful Precursors in Materials Science. *Chem. Soc. Rev.* **2007**, *36* (11), 1770–1787. https://doi.org/10.1039/B614334M.

(20) Rong, W.; Stepan, S.; Smith, R. D. L. Evidence of Variations in Atomic Distribution in Disordered Mixed Metal Hydroxides. *MRS Adv.* **2019**, *4* (33–34), 1843–1850. https://doi.org/DOI: 10.1557/adv.2019.325.

(21) Smith, R. D. L.; Prévot, M. S.; Fagan, R. D.; Trudel, S.; Berlinguette, C. P. Water Oxidation Catalysis: Electrocatalytic Response to Metal Stoichiometry in Amorphous

Metal Oxide Films Containing Iron, Cobalt, and Nickel. *J. Am. Chem. Soc.* **2013**, *135* (31), 11580–11586. https://doi.org/10.1021/ja403102j.

(22) Smith, R. D. L.; Sporinova, B.; Fagan, R. D.; Trudel, S.; Berlinguette, C. P. Facile Photochemical Preparation of Amorphous Iridium Oxide Films for Water Oxidation Catalysis. *Chem. Mater.* **2014**, *26* (4), 1654–1659. https://doi.org/10.1021/cm4041715.

(23) Andronic, L. S.; Hill, R. H. The Mechanism of the Photochemical Metal Organic Deposition of Lead Oxide Films from Thin Films of Lead (II) 2-Ethylhexanoate. *J. Photochem. Photobiol. A Chem.* **2002**, *152* (1–3), 259–265. https://doi.org/10.1016/S1010-6030(02)00020-5.

(24) Dettelbach, K. E.; Salvatore, D. A.; Bottomley, A.; Berlinguette, C. P. Tracking Precursor Degradation during the Photo-Induced Formation of Amorphous Metal Oxide Films. *J. Mater. Chem. A* **2018**, *6* (10), 4544–4549. https://doi.org/10.1039/C7TA10369G.

(25) Lu, H.; Wright, D. S.; Pike, S. D. The Use of Mixed-Metal Single Source Precursors for the Synthesis of Complex Metal Oxides. *Chem. Commun.* **2020**, *56* (6), 854–871. https://doi.org/10.1039/C9CC06258K.

(26) M. Mangiante, D.; D. Schaller, R.; Zarzycki, P.; F. Banfield, J.; Gilbert, B. Mechanism of Ferric Oxalate Photolysis. *ACS Earth Sp. Chem.* **2017**, *1* (5), 270–276. https://doi.org/10.1021/acsearthspacechem.7b00026.

(27) Deacon, G. B.; Phillips, R. J. Relationships between the Carbon-Oxygen Stretching Frequencies of Carboxylato Complexes and the Type of Carboxylate Coordination. *Coord. Chem. Rev.* **1980**, *33* (3), 227–250. https://doi.org/10.1016/S0010-8545(00)80455-5.

(28) Deacon, G. B.; Huber, F.; Phillips, R. J. Diagnosis of the Nature of Carboxylate Coordination from the Direction of Shifts of Carbon□oxygen Stretching Frequencies. *Inorganica Chim. Acta* **1985**, *104* (1), 41–45. https://doi.org/https://doi.org/10.1016/S0020-1693(00)83783-4.

(29) Tao, Y. T. Structural Comparison of Self-Assembled Monolayers of n-Alkanoic Acids on the Surfaces of Silver, Copper, and Aluminum. *J. Am. Chem. Soc.* **1993**, *115* (10), 4350–4358. https://doi.org/10.1021/ja00063a062.

(30) Zhan, G.; Fan, L.; Zhao, F.; Huang, Z.; Chen, B.; Yang, X.; Zhou, S. Fabrication of Ultrathin 2D Cu-BDC Nanosheets and the Derived Integrated MOF Nanocomposites. *Adv. Funct. Mater.* **2019**, *29* (9), 1806720. https://doi.org/https://doi.org/10.1002/adfm.201806720.

(31) Hadjiivanov, K. I.; Panayotov, D. A.; Mihaylov, M. Y.; Ivanova, E. Z.; Chakarova, K. K.; Andonova, S. M.; Drenchev, N. L. Power of Infrared and Raman Spectroscopies to Characterize Metal-Organic Frameworks and Investigate Their Interaction with Guest Molecules. *Chem. Rev.* **2020**. https://doi.org/10.1021/acs.chemrev.0c00487.

(32) Zhang, J.; Zhang, H.; Cao, W.; Pang, Z.; Li, J.; Shu, Y.; Zhu, C.; Kong, X.; Wang, L.; Peng, X. Identification of Facet-Dependent Coordination Structures of Carboxylate Ligands on CdSe Nanocrystals. *J. Am. Chem. Soc.* **2019**, *141* (39), 15675–15683. https://doi.org/10.1021/jacs.9b07836.

(33) Foo, G. S.; Lee, J. J.; Chen, C.-H.; Hayes, S. E.; Sievers, C.; Jones, C. W. Elucidation of Surface Species through in Situ FTIR Spectroscopy of Carbon Dioxide Adsorption on Amine-Grafted SBA-15. *ChemSusChem* **2017**, *10* (1), 266–276. https://doi.org/https://doi.org/10.1002/cssc.201600809.

(34) Lawrie, G.; Keen, I.; Drew, B.; Chandler-Temple, A.; Rintoul, L.; Fredericks, P.; Grøndahl, L. Interactions between Alginate and Chitosan Biopolymers Characterized Using FTIR and XPS. *Biomacromolecules* **2007**, *8* (8), 2533–2541. https://doi.org/10.1021/bm070014y.

(35) Basu Baul, T. S.; Chaurasiya, A.; Duthie, A.; Montes-Tolentino, P.; Höpfl, H. Coordination-Driven Self-Assembly of Macrocycles and 1D or 2D Coordination Polymers Using Heteroditopic Pyridyl-Carboxylate Ligands: The Case Study of 5-[(E)-2-(3-Pyridyl)-1-Diazenyl]-2-Hydroxybenzoate in Combination with {RnSn} (n = 2 and 3). *Cryst. Growth Des.* **2019**, *19* (11), 6656–6671. https://doi.org/10.1021/acs.cgd.9b01045.

(36) Otero, V.; Sanches, D.; Montagner, C.; Vilarigues, M.; Carlyle, L.; Lopes, J. A.; Melo, M. J. Characterisation of Metal Carboxylates by Raman and Infrared Spectroscopy in Works of Art. *J. Raman Spectrosc.* **2014**, *45* (11–12), 1197–1206. https://doi.org/https://doi.org/10.1002/jrs.4520.

(37) Lorenz-Fonfria, V. A. Infrared Difference Spectroscopy of Proteins: From Bands to

Bonds. *Chem. Rev.* **2020**, *120* (7), 3466–3576. https://doi.org/10.1021/acs.chemrev.9b00449.

(38) Noda, I. Two-Dimensional Infrared Spectroscopy. *J. Am. Chem. Soc.* **1989**, *111* (21), 8116–8118. https://doi.org/10.1021/ja00203a008.

(39) Noda, I. Generalized Two-Dimensional Correlation Method Applicable to Infrared, Raman, and Other Types of Spectroscopy. *Appl. Spectrosc.* **1993**, *47* (9), 1329–1336. https://doi.org/10.1366/0003702934067694.

(40) Noda, I. Scaling Techniques to Enhance Two-Dimensional Correlation Spectra. *J. Mol. Struct.* **2008**, *883–884*, 216–227. https://doi.org/10.1016/j.molstruc.2007.12.026.

(41) Noda, I. Techniques Useful in Two-Dimensional Correlation and Codistribution Spectroscopy (2DCOS and 2DCDS) Analyses. *J. Mol. Struct.* **2016**, *1124*, 29–41. https://doi.org/10.1016/j.molstruc.2016.01.089.

(42) Lasch, P.; Noda, I. Two-Dimensional Correlation Spectroscopy (2D-COS) for Analysis of Spatially Resolved Vibrational Spectra. *Appl. Spectrosc.* **2019**, *73* (4), 359–379. https://doi.org/10.1177/0003702818819880.

(43) Sutton, C. C. R.; da Silva, G.; Franks, G. V. Modeling the IR Spectra of Aqueous Metal Carboxylate Complexes: Correlation between Bonding Geometry and Stretching Mode Wavenumber Shifts. *Chem. – A Eur. J.* **2015**, *21* (18), 6801–6805. https://doi.org/10.1002/chem.201406516.

(44) H. Hill, R.; L. Blair, S. *An Inorganic Approach to Photolithography: The Photolithographic Deposition of Dielectric Metal Oxide Films*; 2009. https://doi.org/10.1021/bk-1998-0706.ch005.

(45) E. Jackson, V.; R. Felmy, A.; A. Dixon, D. Prediction of the PKa's of Aqueous Metal Ion +2 Complexes. *J. Phys. Chem. A* **2015**, *119* (12), 2926–2939. https://doi.org/10.1021/jp5118272.

(46) Galstyan, G.; Knapp, E.-W. Computing PK_A Values of Hexa-Aqua Transition Metal Complexes. *J. Comput. Chem.* **2015**, *36* (2), 69–78. https://doi.org/10.1002/jcc.23764.

(47) Gilson, R.; Durrant, M. C. Estimation of the PK_a Values of Water Ligands in Transition Metal Complexes Using Density Functional Theory with Polarized Continuum Model

Solvent Corrections. *Dalt. Trans.* **2009**, No. 46, 10223–10230. https://doi.org/10.1039/B911593E.

(48) Trasatti, S. Work Function, Electronegativity, and Electrochemical Behaviour of Metals. *J. Electroanal. Chem. Interfacial Electrochem.* **1972**, *39* (1), 163–184. https://doi.org/10.1016/S0022-0728(72)80485-6.

(49) Doyle, A.; Felcman, J.; Gambardella, M. T. do P.; Verani, C. N.; Tristão, M. L. B. Anhydrous Copper(II) Hexanoate from Cuprous and Cupric Oxides. The Crystal and Molecular Structure of $Cu_2(O_2CC_5H_{11})_4$. *Polyhedron* **2000**, *19* (26–27), 2621–2627. https://doi.org/10.1016/S0277-5387(00)00568-4.

For Table of Contents Only

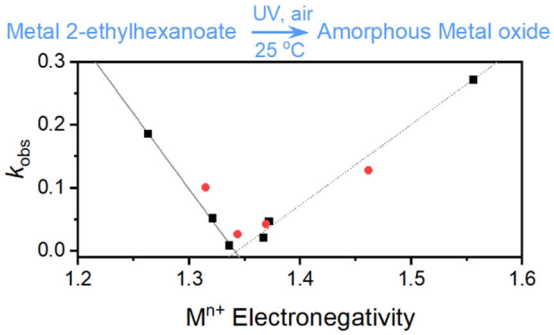

Two-dimensional generalized correlation spectroscopy (2D-COS) is demonstrated to be a powerful tool for studying complex solid-state reaction mechanisms. Infrared spectra acquired throughout a photochemically-induced decomposition reaction enhanced spectroscopic resolution, enabling analysis of binding modes as a function of reaction time. Ligands bound as chelates are shown to be essential for decomposition, with data correlations suggesting that M-O bond strength and protonation state control reaction kinetics.